NANO · MICRO small
www.small-journal.com

Synergistic Metal-Support Interactions in Au/GaN Catalysts for Photoelectrochemical Nitrate Reduction to Ammonia

Wan Jae Dong, Jan Paul Menzel, Zhengwei Ye, Zhuoran Long, Ishtiaque Ahmed Navid, Victor S. Batista, and Zetian Mi**

Metal-support interactions are crucial in the electrochemical synthesis of ammonia (NH_3) from nitrate (NO_3^-) reduction reaction, enabling efficient NH_3 production under mild conditions. However, the complexity of the reaction pathways often limits efficiency. Here, a photoelectrochemical system composed of gold (Au) nanoclusters supported on gallium nitride (GaN) nanowires is introduced, grown on a n^+-p Si wafer, for selective reduction of NO_3^- to NH_3 under solar illumination. NO_3^- ions are preferentially adsorbed and reduced to nitrite (NO_2^-) on the GaN nanowires, which then transfer to adjacent Au nanoclusters to complete the NH_3 synthesis. This mechanism is confirmed by both experimental data and theoretical calculations. Optimizing the surface coverage and size of Au nanoclusters on the GaN nanowires significantly enhanced catalytic activity compared to that on planar n^+-p Si photoelectrodes, achieving a faradaic efficiency of 91.8% at −0.4 V_{RHE} and a high NH_3 production rate of 131.1 μmol cm^{-2} h^{-1} at −0.8 V_{RHE}. These findings highlight the synergetic effect between metal co-catalysts and semiconductor supports in designing photoelectrodes for multi-step NO_3^- reduction.

1. Introduction

Ammonia (NH_3) is a critical feedstock for fertilizers and a promising carbon-free hydrogen carrier, easily stored in liquid form.[1,2] Currently, industrial NH_3 production relies on the energy-intensive and carbon-emissive Harber–Bosch process, which operates under high temperatures and pressure.[3,4] As a clear alternative, the electrochemical nitrogen (N_2) reduction reaction in aqueous electrolytes allows for NH_3 synthesis under milder conditions.[5–7] However, the high dissociation energy of the N≡N bond (941 kJ mol^{-1}) limits both the selectivity and efficiency. In contrast, the electrochemical nitrate reduction reaction (NO_3^-RR) is more feasible due to the significantly lower dissociation energy of the N=O bond (204 kJ mol^{-1}) and the much higher solubility of NO_3^- in aqueous electrolytes–≈40000 times greater than that of N_2.[8,9] Furthermore, the abundance of NO_3^- in wastewater makes its reduction a sustainable approach to NH_3 synthesis, while also providing an effective solution for mitigating environmental pollution through runoff purification.

The NO_3^-RR to NH_3 is a complex eight-electron process ($NO_3^- + 9H^+ + 8e^- \rightarrow NH_3 + 3H_2O$) involving 9 protons ($H^+$) for deoxygenation and hydrogenation steps.[10] Previous studies have explored various metal-based catalysts, including Cu-PTCDA,[11] strained Ru nanoclusters,[12] Fe single-atom catalysts,[13,14] and strained Bi,[15] to enhance the faradaic efficiency for NH_3 (FE_{NH3}) and reduce the overpotential. While several catalysts have demonstrated success for NO_3^-RR, detailed mechanistic studies remain limited.

Recently, binary metal compound catalysts such as CuNi,[16] CuCoSP,[17] Rh@Cu,[18] and $NiCo_2O_4$[19] have shown improved NH_3 production compared over their single-metal counterparts, due to metal-support interactions and the transfer of reaction intermediates between multiple active phases. These heterogeneous catalysts enhance reaction kinetics and lower thermodynamic barriers by modulating the binding energy of adsorbates on the catalytic surface. For example, Rh clusters on Cu surfaces provide sufficient hydrogen, activating the hydrogenation process and promoting selective NH_3 production.[18] Similarly, $Co(OH)_2$ aids in the hydrogenation of adsorbed NO_3^- in the CoP/$Co(OH)_2$ catalytic system.[20]

W. J. Dong, Z. Ye, I. A. Navid, Z. Mi
Department of Electrical Engineering and Computer Science
University of Michigan
1301 Beal Avenue, Ann Arbor, Michigan 48109, USA
E-mail: ztmi@umich.edu

W. J. Dong
Department of Integrative Energy Engineering
Graduate School of Energy and Environment (KU-KIST Green School)
College of Engineering
Korea University
Seoul 02841, Republic of Korea

J. P. Menzel, Z. Long, V. S. Batista
Department of Chemistry
Yale University
New Haven, Connecticut 06520–8107, USA
E-mail: victor.batista@yale.edu

The ORCID identification number(s) for the author(s) of this article can be found under https://doi.org/10.1002/smll.202412089

DOI: 10.1002/smll.202412089

In microorganisms, NH_3 synthesis from NO_3^-RR occurs through two tandem reactions: 1) NO_3^- reduction to NO_2^- by nitrate reductase, and 2) NO_2^- conversion to NH_3 by nitrite reductase or nitrogenase.[21–23] This tandem process has been artificially replicated using CuCoSP, where Cu/CuO_x phases reduce NO_3^- to NO_2^-, and the NO_2^- intermediate is transferred and converted to NH_3 on Co/CoO phases.[17] The design strategy of combining dual active sites for tandem reactions can also be applied to metal-semiconductor systems. Successfully designing such systems could leverage photon-to-electron conversion in semiconductors to further reduce the overpotential required for NO_3^-RR, as demonstrated in previous energy-efficient photoelectrochemical reactions.[24–31]

In this study, we investigated the synergistic metal-support interactions between Au nanoclusters (NCs) and GaN nanowires (NWs) grown on an n^+-p Si wafer for photoelectrochemical (PEC) NO_3^-RR to NH_3 under simulated solar light. By optimizing the surface coverage and size of Au NCs on GaN NWs, we achieved rapid adsorption and reduction of NO_3^- to NO_2- on the GaN NWs, followed by efficient NH_3 generation on the Au NCs. This optimization led to a significant increase in the Faradaic efficiency for NH_3 (FE_{NH3}) reaching 91.8% at −0.4 V vs reversible hydrogen electrode (V_{RHE}). Density functional theory (DFT) calculations corroborated the experimental findings, showing that NO_3^- is reduced to NO_2^- on the GaN surface and displaced by the remaining NO_3^-, while NO_2^- is further reduced to NH_3 on the Au NCs. The sequential reduction reactions occurring on the adjacent Au and GaN surfaces resulted in a high production rate of NH_3 (Y_{NH3}) of 131.1 μmol cm^{-2} h^{-1} at −0.8 V_{RHE} with selective NH_3 generation (FE_{NH3} > 90%) sustained for 8 h at −0.4 V_{RHE}. This work offers valuable insights for designing metal/semiconductor systems to achieve high-efficiency PEC NO_3^-RR to NH_3 under solar illumination.

2. Results And Discussion

Au/GaN/Si photoelectrodes were fabricated using plasma-assisted molecular beam epitaxy to grow GaN NWs on an n^+-p Si wafer, followed by photodeposition of Au NCs as described in the experimental section. Scanning electron microscopy (SEM) studies confirmed the vertical growth of GaN NWs on the planar n^+-p Si wafer (**Figure 1a**). The GaN NWs measured ≈450 nm in length and 50 nm in diameter. Three variations of Au/GaN/Si photoelectrodes were prepared by adjusting the volume of 0.4 M $HAuCl_4$ precursor solution used during photodeposition, denoted as Au#/GaN/Si, where # indicates the precursor solution volume. As the precursor volume increased from 1 to 100 μL, the size of Au NCs increased, particularly in the upper region of the GaN NWs (Figure S1, Supporting Information). The microstructure of GaN NWs and Au NCs was further examined using a high-angle annular dark-field scanning transmission electron microscopy (HAADF-STEM) (Figure 1b; Figure S2, Supporting Information). Due to the significant atomic number difference between Au (79) and Ga (31), Z-contrast imaging revealed locally aggregated Au NCs on both the top and sidewalls of the GaN NWs. Elemental mapping by energy-dispersive X-ray spectroscopy (EDS) showed a uniform distribution of Ga (blue), and N (green) across the GaN NWs, while Au NCs (pink), ranging from 2 to 20 nm in size, were sparsely distributed on the GaN surface, indicating a non-uniform decoration of Au NCs on the GaN NWs. The non-uniform distribution of Au NCs can be attributed to preferential photodeposition at the tips of GaN NWs, where enhanced light absorption and higher photo-excited electron density promote localized growth. In future work, fine-tuning the photodeposition parameters, such as light wavelength and deposition time, will be pursued to achieve the formation of more uniformly distributed Au NC.

X-ray photoelectron spectroscopy (XPS) was used to analyze the surface chemical composition of the photoelectrodes. The Ga $2p_{3/2}$ XPS spectrum was deconvoluted into a dominant Ga—N bond peak at 1116.8 eV and a minor Ga—O bond peak at 1118.0 eV (Figure 1c).[32] As the amount of Au NCs increased, the intensity of the Ga $2p_{3/2}$ signal diminished due to the screening effect of the Au NCs, which blocked photoelectrons emitted from the GaN surface. Similarly, the N 1s XPS spectrum (Figure 1d) was split into a major N—Ga bond at 396.7 eV and a minor N—O bond at 398.1 eV,[33] both of which showed decreasing intensity with increasing Au NC loading. The Au NCs exhibited the metallic Au^0 phase, with binding energies at 83.4 and 87.1 eV, alongside a trace amount of Au^+ at 84 and 87.7 eV (Figure 1e). As the Au loading increased, the intensity of the Au 4f peaks increased and the Au 4f peak shifted toward a higher binding energy, approaching the reference value of 84 eV for bulk Au $4f_{7/2}{}^0$.[34] This indicates that smaller Au NCs have weaker electron binding compared to bulk Au, primarily due to electron transfer from GaN NWs to Au NCs at the interface. This interfacial charge transfer is particularly pronounced for smaller Au NCs, as shown by the shifts of Ga and N peaks to higher binding energies and Au peaks to lower binding energies in the XPS spectra. As the size of the Au NCs increases, thicker Au layers gradually screen the interfacial charge transfer effect, leading to bulk-like electronic properties.

The surface atomic ratios of Au with respect to Ga and N, calculated from the XPS data, were 0.09, 1.06, and 8.91 for Au1/GaN, Au10/GaN, and Au100/GaN, respectively (Figure 1f).

X-ray diffraction (XRD) pattern of GaN/Si revealed a distinct GaN (002) peak [JCPDS #02-1078], confirming GaN NWs were single crystals (Figure 1g). The Au (111) peak was only detected in the Au100/GaN/Si sample, indicating that the crystallite size of the Au NCs was sufficiently large for XRD detection [JCPDS #04-0784]. In contrast, smaller Au NCs such as Au1 and Au10 samples, likely had a higher proportion of surface-exposed Au atoms, particularly at terrace sites, compared to bulk crystal facets. This increased surface exposure, especially on high-index crystal planes, can enhance catalytic properties by providing a greater number of active sites, potentially enhancing the reactivity.

PEC NO_3^-RR was performed in an H-type cell using simulated AM1.5G 1-sun solar light, with the light sources positioned perpendicular to the planar n^+-p Si photoelectrodes. Linear sweep voltammetry (LSV) curves were recorded in 0.1 M K_2SO_4 with varying KNO_3 concentrations (0, 0.02, 0.1, 0.5, and 1 M). As the NO_3^- concentration increased from 0 to 1 M, the onset potential (V_{onset}) at −1.0 mA cm^{-2} for GaN/Si shifted significantly from −0.63 to −0.21 V_{RHE} (**Figure 2a**), indicating that GaN/Si exhibits higher catalytically activity for NO_3^-RR compared to the hydrogen evolution reaction (HER). However, as the loading of Au NCs increased, the difference in V_{onset} between electrolytes with different NO_3^- concentrations diminished (Figure S3, Supporting

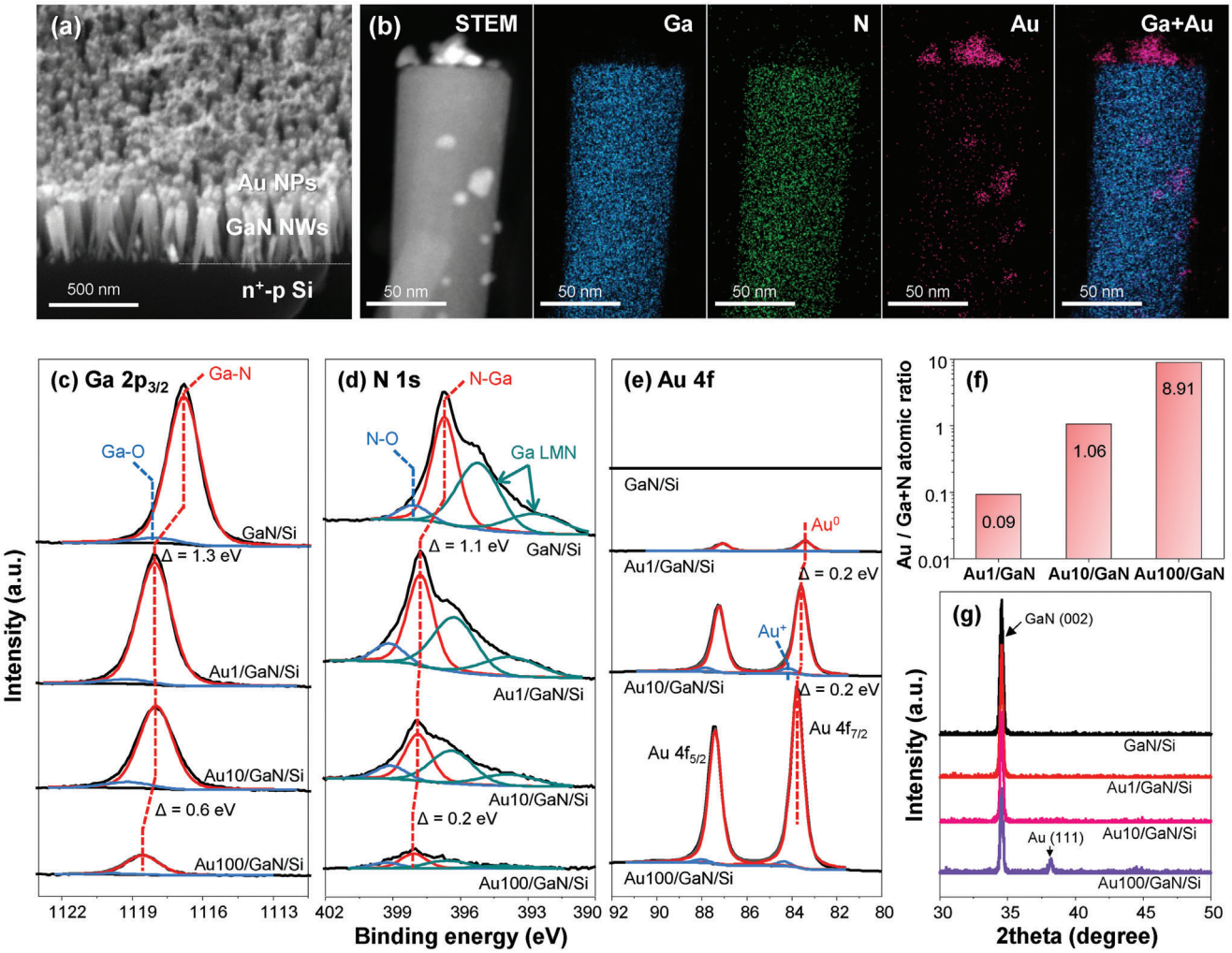

Figure 1. a) 45°-tilt-view SEM image of Au10/GaN/Si. b) STEM image and EDS elemental maps of Au/GaN. Ga (blue) and N (green) from GaN NWs were uniformly distributed while Au (pink) from Au NCs was aggregated on the upper region of GaN NWs. XPS spectra of c) Ga $2p_{2/3}$, d) N 1s, e) Au 4f for GaN/Si, Au1/GaN/Si, Au10/GaN/Si, and Au100/GaN/Si. f) Au/Ga+N ratio calculated from XPS analysis. g) XRD patterns of photoelectrodes.

Information). Eventually, Au100/GaN/Si showed minimal variation in LSV curves regardless of NO_3^- concentration, with V_{onset} ranging between −0.17 to −0.21 V_{RHE} (Figure 2b,c). These results suggest competitive behavior between NO_3^-RR and HER on the Au 100 co-catalyst. Additionally, the saturated photocurrent density ($J_{saturation}$) at −2 V_{RHE} decreased from −41.0 to −16.8 mA cm^{-2} as the Au NCs loading increased, likely due to the Au NCs blocking incident light and reducing light absorption by the underlying n^+-p Si photoelectrode (Figure 2d).[35] Under dark conditions, all photoelectrodes exhibited a current density close to zero, attributed to the absence of photon-induced charge carrier generation. This indicates that the reduction reactions on the photoelectrodes are entirely reliant on photo-generated charge carriers. To further investigate photovoltage generation by photoelectrode, we fabricated an electrochemical reaction electrode by growing GaN NWs on an electrically conductive n-type silicon substrate (n-Si) and loading it with Au NCs. LSV curves measured in 0.1 M K_2SO_4 with 0.1 M KNO_3 electrolyte revealed that the onset potential for the Au/GaN/n-Si electrode under dark conditions was ≈0.5 V more negative compared to the Au/GaN/n^+-p Si photoelectrode under illuminated conditions (Figure S4, Supporting Information). This difference highlights the role of underlying n^+-p Si in reducing the voltage requirement by effectively harnessing solar energy.

Faradaic efficiencies (FEs) for GaN/Si, Au1/GaN/Si, Au10/GaN/Si, and Au100/GaN/Si were assessed in electrolytes with varying NO_3^- concentrations at −0.4 V_{RHE} (Figure 2e,f). Concentrations of NH_3, NO_2^-, and N_2H_4 products were determined via spectrocolorimetric analysis (Figure S5, Supporting Information). In 0.1 M K_2SO_4 (without NO_3^-), all photoelectrodes exhibited selective HER with FE_{H2} > 95% (Figure S6, Supporting Information). Upon introducing 0.02 M KNO_3, the production of NH_3, NO_2^-, and N_2H_4 was observed, with Au10/GaN/Si achieving the highest FE_{NH3} of 59.5% (Figure 2e). Notably, GaN/Si effectively suppressed HER (FE_{H2} < 3%) and selectively converted NO_3^- into NO_2^- (FE_{NO2-} > 80%), even with 0.02 M NO_3^- (Figure 2f; Figure S7, Supporting Information). However, H_2 production remained significant on Au/GaN/Si,

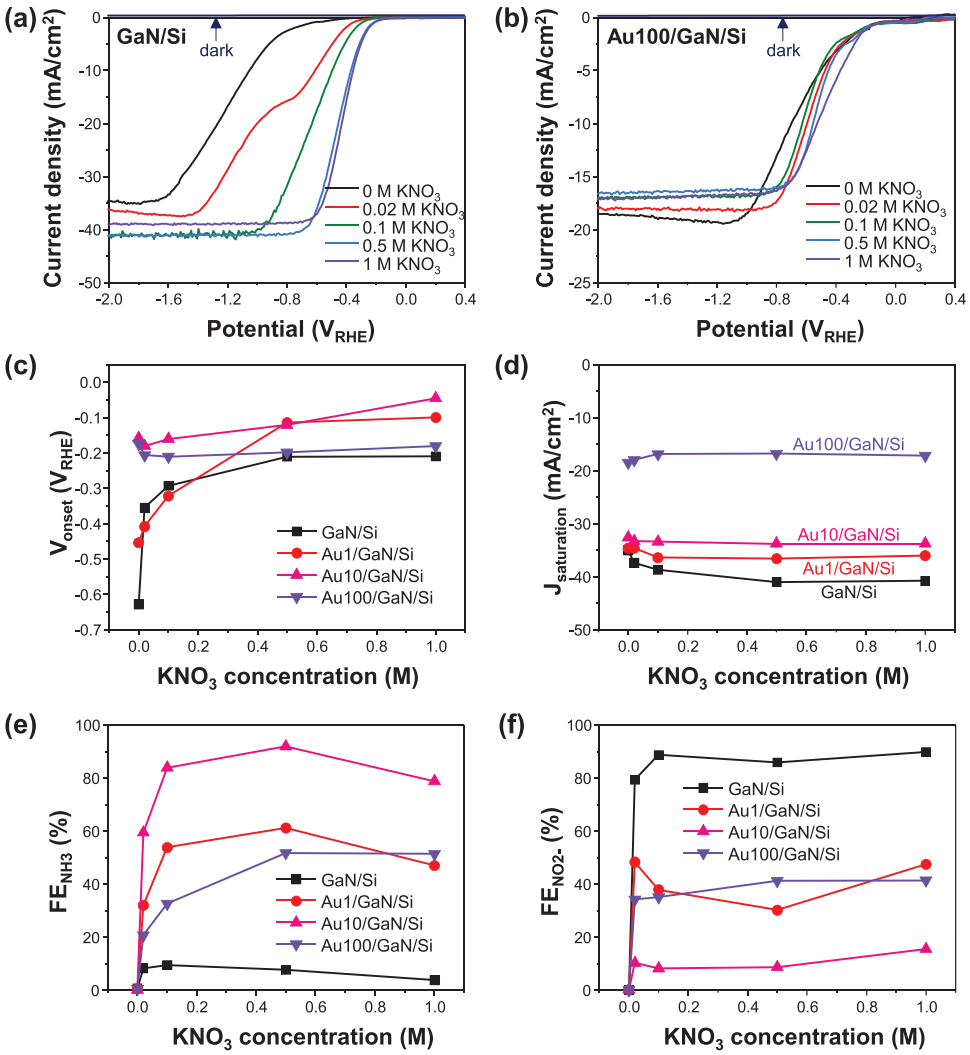

Figure 2. LSV curves of a) GaN/Si and b) Au100/GaN/Si measured in 0.1 M K_2SO_4 with KNO_3 concentrations of 0, 0.02, 0.1, 0.5, and 1 M. The measurement was conducted under 1-sun-light illumination. Under dark conditions, the photoelectrodes were tested in 0.1 M K_2SO_4 electrolyte. Plots of c) V_{onset} at −1.0 mA cm^{-2} and d) $J_{saturation}$ at −2 V_{RHE} with KNO_3 concentration. Faradaic efficiency of e) NH_3 and (f) NO_2^- for GaN/Si, Au1/GaN/Si, Au10/GaN/Si, and Au100/GaN/Si measured in 0.1 M K_2SO_4 with different KNO_3 concentration at −0.4 V_{RHE}. Au10/GaN/Si represented the highest FE_{NH3} (91.8%) among the tested samples.

with the highest FE_{H2} of 41.6% observed for Au100/GaN/Si (Figure S6, Supporting Information). As NO_3^- concentration increased, the FE_{NH3} for Au/GaN/Si gradually rose (Figures S8–S10, Supporting Information). Au10/GaN/Si demonstrated the optimal balance of Au coverage, achieving a maximum FE_{NH3} of 91.8% at 0.5 M NO_3^-, highlighting the importance of fine-tuning Au/GaN metal-support interactions to maximize catalytic performance.

To further investigate metal-support interactions, we fabricated planar n^+-p Si and Au-coated n^+-p Si (Au10/Si) photoelectrodes. The LSV curve of Au10/Si exhibited a more positive V_{onset} = −0.41 V_{RHE} compared to Si (−0.81 V_{RHE}) in 0.1 M K_2SO_4 with 0.5 M KNO_3 (**Figure 3a**). However, both remained more negative than those of GaN/Si or Au/GaN/Si, highlighting GaN NWs as promising platforms for loading Au co-catalysts in NO_3^-RR. Additionally, the $J_{saturation}$ of GaN/Si was ≈1.5 times higher than planar Si, attributed to the antireflective properties of GaN NWs.[36]

The influence of the applied potential on FE and production rates was evaluated for Si (Figure S11, Supporting Information), Au/Si (Figure S12, Supporting Information), GaN/Si (Figure S13, Supporting Information), Au10/GaN/Si (Figure S14, Supporting Information), and Au100/GaN/Si (Figure S15, Supporting Information), with a summary of FE_{NH3} shown in Figure 3b. Planar Si achieved a FE_{NH3} of 36.3% at −0.8 V_{RHE}, while Au deposition on Si (Au/Si) marginally increased the NH_3 selectivity (FE_{NH3} = 47.2% at −0.8 V_{RHE}). In contrast, GaN/Si predominantly produced NO_2^- (FE_{NO2-} > 90% at potential < −0.3 V_{RHE}), with low NH_3 (FE_{NH3} < 16%) and N_2H_4 (FE_{N2H4} < 3%) selectivities. GaN NWs effectively reduce NO_3^- to NO_2^-, which was desorbed from the photoelectrode surface before further

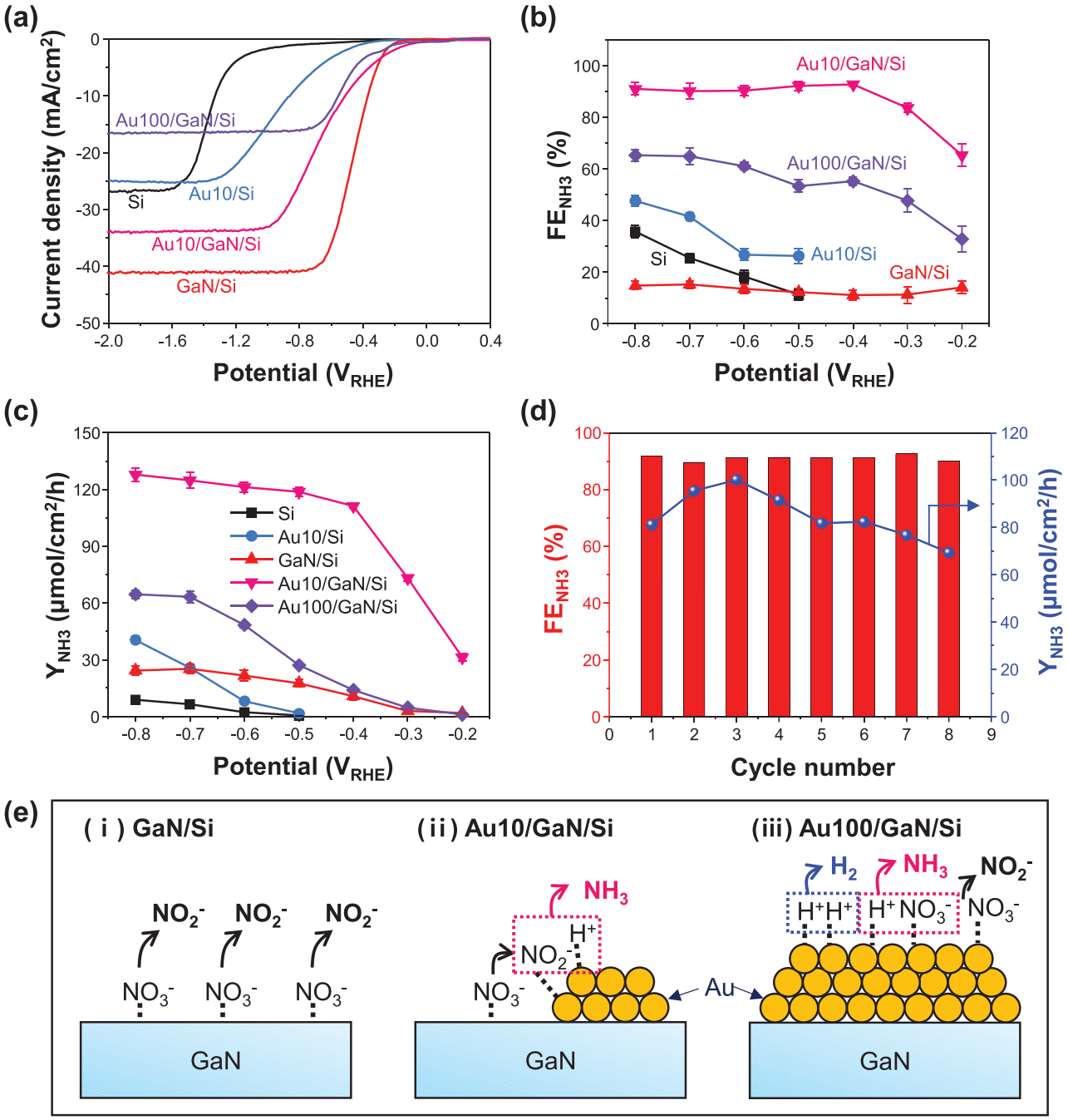

Figure 3. LSV curves of Si, Au10/Si, GaN/Si, Au10/GaN/Si, and Au100/GaN/Si measured in 0.1 M K_2SO_4 with 0.5 M KNO_3. b) Faradaic efficiency and c) production rate of NH_3 plotted as a function of cathodic potentials from −0.2 to −0.8 V_{RHE}. NH_3 production was measured three times, and the mean values along with their standard deviations are represented as error bars. Au10/GaN/Si had the widest potential window (−0.4 to −0.8 V_{RHE}) for high FE_{NH3} > 90% and achieved the best Y_{NH3} = 131.1 μmol cm^{-2} h^{-1} at −0.8 V_{RHE}. d) FE_{NH3} and Y_{NH3} for 8 cycles of reaction. Each cycle was performed for 1 h at −0.4 V_{RHE}. e) Schematic illustrations of adsorption of NO_3^- and NO_3^- reduction reaction on (i) GaN/Si, (ii) Au10/GaN/Si, and (iii) Au100/GaN/Si. The dashed line represents the adsorption of molecules and the arrow line indicates the reduction reaction.

reduction. Au10/GaN/Si demonstrated a broad potential window (−0.4 to −0.8 V_{RHE}) for selective NH_3 production (FE_{NH3} > 90%). As a result, Au10/GaN/Si exhibited the highest FE_{NH3} among the tested photoelectrodes, achieving NH_3 production rates (Y_{NH3}) of 110 μmol cm^{-2} h^{-1} at −0.4 V_{RHE} and 131.1 μmol cm^{-2} h^{-1} at −0.8 V_{RHE} (Figure 3c). The FE_{NH3} and Y_{NH3} values for Au10/GaN/Si outperformed recent photoelectrodes and were comparable to state-of-the-art electrocatalysts (Table S1, Supporting Information).

We assessed the stability of Au10/GaN/Si over 8 cycles in 0.1 M K_2SO_4 with 0.5 M KNO_3 (Figures 3d). Each cycle was run for 1 h at a constant potential of −0.4 V_{RHE}, with fresh electrolytes

introduced for every cycle. Chronoamperometric curve (Figure S16a, Supporting Information) revealed an initial high photocurrent density, which gradually decreased over 1 h of reaction. This behavior was likely due to the depletion of NO_3^- concentration near the surface as the reaction progresses, and the accumulation of by-products that poisoned the surface. Upon replacing the electrolyte with a fresh solution, the photocurrent density was restored to its initial high level, confirming that the observed decrease was primarily due to changes in the reaction environment rather than irreversible degradation of the photoelectrode. Throughout the 8 cycles, a high NH_3 faradaic efficiency (FE_{NH3} > 90%) was consistently maintained (Figure S16b, Supporting Information). The NH_3 production rate (Y_{NH3}) increased to 100.1 μmol cm^{-2} h^{-1} during the first 3 cycles but gradually declined to 69.3 μmol cm^{-2} h^{-1} over the last 5 cycles (Figure S16c, Supporting Information). This reduction in Y_{NH3} was attributed to the detachment of Au NCs from the GaN NWs (Figure S17, Supporting Information). Although Au NCs remained on the surface of GaN NWs after 8 cycles, the Au/Ga+N ratio dropped from 1.06 to 0.47, indicating a loss of Au NCs. To address this issue, incorporating protective layers,[37,38] or applying pre- or post-treatments[30] could be explored to enhance the interfacial binding between Au NCs and GaN NWs, thereby improving the long-term stability of the photoelectrode. Despite this challenge, Au10/GaN/Si remained a promising photoelectrode for selective and sustained NH_3 production with extended stability. Additionally, isotope labeling experiments confirmed that NH_3 originated from NO_3^- rather than from the nitrogen of GaN, demonstrating that GaN NWs remained chemically stable during the PEC NO_3^- RR (Figure S18, Supporting Information).

Our findings highlight that initial NO_3^- adsorption is critical for selective NH_3 production. On the GaN surface, NO_3^- primarily adsorbs and is converted to NO_2^-, which desorbs without further reduction, leading to a high FE_{NO2-} > 80% (Figure 3e). However, when a moderate amount of small Au NCs was deposited on the GaN surface (Au10/GaN/Si), the NO_2^- produced on GaN migrates to nearby Au sites where further reduction to NH_3 occurs via deoxygenation and hydrogenation with H^+, resulting in high FE_{NH3} > 90% (Figure S19a, Supporting Information). In contrast, larger Au crystallites with higher surface coverage on GaN (Au100/GaN/Si) impaired NO_3^- adsorption (Figure S19b, Supporting Information) and reduced the number of Au-GaN active sites. This led to competition between NO_3^-RR and the hydrogen evolution reaction (HER), causing a drop in FE_{NH3} to below 70%.

The mechanistic insights from DFT calculations support these observations (see free energies of reactants, products, and intermediates in Tables S2 and S3, Supporting Information). Previous research on photoelectrochemical NO_3^- reduction on GaN nanowires has demonstrated that NO_2^- is the primary product.[39] This is because the reduction of NO_3^- to NO_2^- is thermodynamically favorable, requiring only one endergonic electron transfer step with an energy of +0.29 eV (as reported in ref. [39]), which is easily provided by the photo-excited electrons. In contrast, the reduction of NO_2^- to NO to form the first intermediate toward reduction to NH_3 requires significantly more energy (+0.65 eV) (**Figure 4a**). Additionally, GaN shows a stronger affinity for NO_3^- over NO_2^-, with the binding free energy of NO_3^- being more favorable by ≈−0.09 eV. This preferential binding of NO_3^- leads to the displacement of NO_2^-, which explains why NO_2^- is the main product of NO_3^- reduction. Thus, the combination of lower energy requirements for NO_3^- reduction and the stronger binding affinity of NO_3^- over NO_2^- results in NO_2^- being expelled as the main product during NO_3^- reduction.

On the Au surface (Figure S20, Supporting Information), the binding preference between NO_3^- and NO_2^- is reversed: we find that NO_2^- exhibits a more negative binding free energy than NO_3^- by ≈−0.30 eV on the Au (211) surface (Figure S21, Supporting Information). This suggests that once NO_2^- has been formed, it preferentially binds to Au making the initial adsorption of NO_3^- on Au (211) more difficult. Additionally, the reduction of NO_3^- to NO_2^- on Au involves an endergonic step of +0.30 eV during the conversion of $^*NO_2$ to $^*NO_2^-$ (Figure S22, Supporting Information), indicating that NO_3^- reduction to NO_2^- on Au is relatively slow and easily outcompeted by GaN. It is also worth noting that while both NO_2^- and NO_3^- chemisorption on the inert Au surface is entropically disfavored in a vacuum, the chemisorption of NO_2^- is more favorable than that of NO_3^-.

In contrast, the further reduction of NO_2^- is strongly favored on Au (Figure 4b). This process involves a transition in the binding mode from $^*ONO^{-*}$ (where NO_2^- binds via its two oxygen atoms to the Au step) to the $^*NO_2^-$ (where nitrogen binds to the Au step, with one of the oxygen atoms pointing down and adsorbing onto the lower terrace) (Figure S23, Supporting Information). This switch from oxygen to nitrogen binding is crucial for the dissociation of the second N=O bond and has been extensively investigated in other metal systems.[40] Here, a minimal free energy of 0.01 eV –easily surmountable thermally– enables irreversible bond dissociation to $^*NO$ and $^*OH$ intermediates on the surface. The subsequent removal of $^*OH$ through protonation, coupled with the reduction of the oxidized Au surface, is highly exergonic.

Further reduction steps to $^*NHO$, $^*NHOH$, $^*NH$, and $^*NH_2$, culminating in the release of NH_3 are also exergonic, leading to complete reduction to NH_3 once NO_2^- dissociates. These computational findings align well with experimental observations, explaining why Au NCs without GaN show low NH_3 production yield–since little NO_2^- is formed and made available for further reduction – and why GaN alone exhibits high faradaic efficiency toward NO_2^- rather than to NH_3. High and selective production of NH_3 is observed only when GaN and Au are used together, with GaN reducing NO_3^- to NO_2^-, which desorbs and undergoes further reduction on Au, ultimately forming NH_3.

3. Conclusions

In conclusion, we have demonstrated the unique metal-support interactions between Au NCs and GaN NWs, which act as synergetic catalytic sites for PEC NO_3^-RR to NH_3. In this binary system, NO_3^- is preferentially reduced to NO_2^- on GaN NWs, while NO_2^- is subsequently converted to NH_3 on adjacent Au NCs. The sequential reduction of NO_3^- and NH_3 synthesis occurs across two adjacent Au/GaN phases, making the optimization of Au NCs coverage on GaN NWs crucial for achieving selective NH_3 production. As a result, the designed Au/GaN/Si photoelectrode exhibited excellent performance, with faraday efficiency (FE_{NH3}) of 91.8% at −0.4 V_{RHE} and a high production rate (Y_{NH3}) of 131.1 μmol cm^{-2} h^{-1} at −0.8 V_{RHE}, with no significant degradation over 8 h. A deeper understanding and precise design of the electronic and catalytic properties at the metal-semiconductor

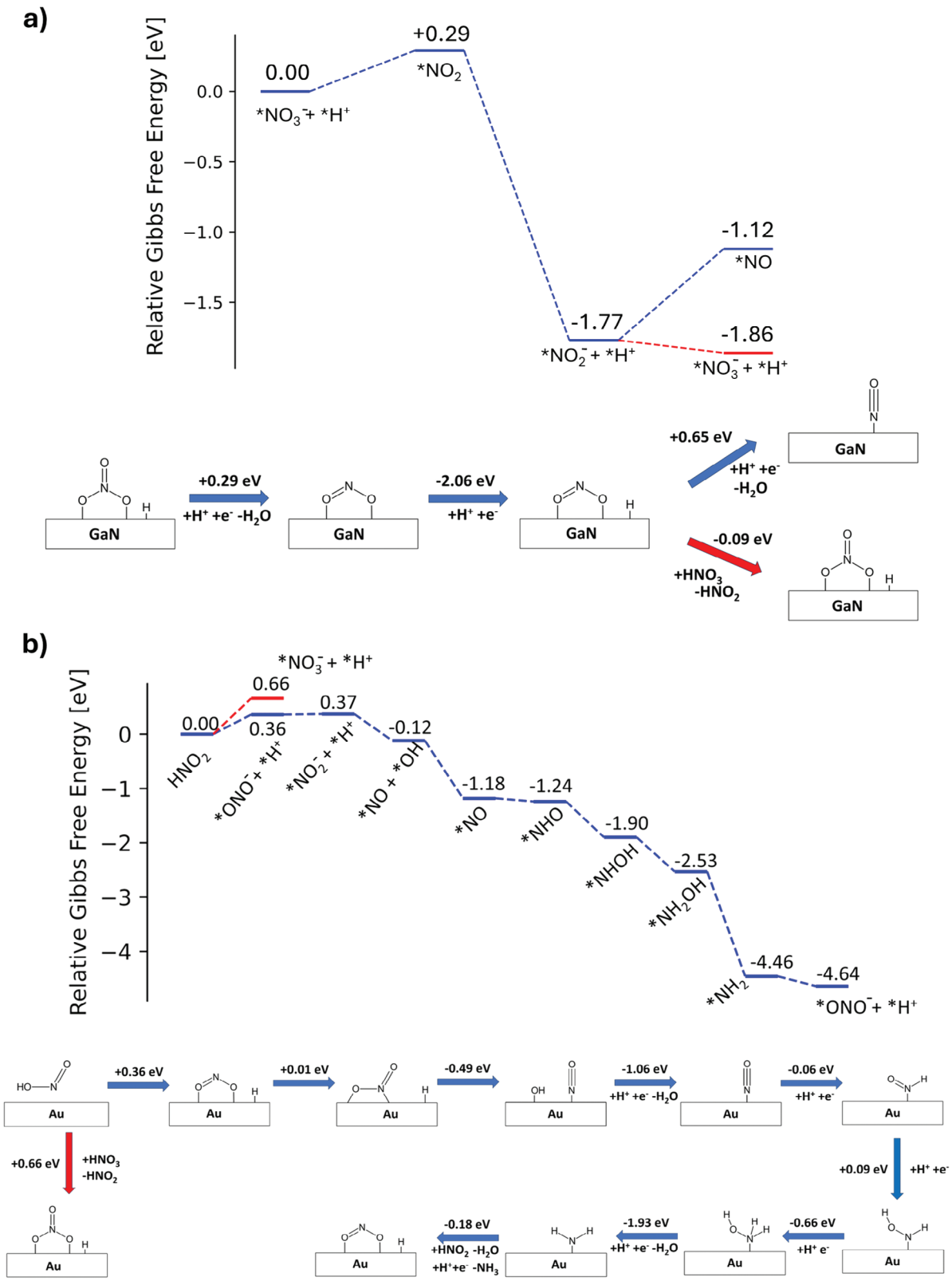

Figure 4. a) Relative free energies of NO_3^- reduction to NO_2^- on GaN surfaces, with values taken from ref. [39]. After reduction to NO_2^-, the reduction to NO (and then further to NH_3) shown in blue requires high reductive potentials, while expulsion of the NO_2^- by incoming NO_3^- is favorable (red), making NO_2^- the main product in PEC NO_3^- reduction on GaN. b) Relative free energies of NO_2^- reduction on Au (211) surface. Expulsion of the NO_2^- by NO_3^- (red) is unfavorable, meaning NO_2^- can be fully reduced toward NH_3.

interface will likely enable more efficient solar-driven NO_3^-RR to NH_3.

Supporting Information

Supporting Information is available from the Wiley Online Library or from the author.

Acknowledgements

W.J.D. and J.P.M. contributed equally to this work. This work was supported by the United States Army Research Office Award W911NF2110337.

Conflict of Interest

Some IP related to this work was licensed to NS Nanotech, Inc. and NX Fuels, Inc., which were co-founded by Z. Mi. The University of Michigan and MI have a financial interest in the company.

Data Availability Statement

The data that support the findings of this study are available from the corresponding author upon reasonable request.

Keywords

ammonia, Au, GaN, metal-support interaction, nitrate reduction

Received: December 12, 2024
Revised: January 21, 2025
Published online:

[1] A. Good, *Science* **2018**, *359*, 869.
[2] D. R. MacFarlane, P. V. Cherepanov, J. Choi, B. H. Suryanto, R. Y. Hodgetts, J. M. Bakker, F. M. F. Vallana, A. N. Simonov, *Joule* **2020**, *4*, 1186.
[3] G. Soloveichik, *Nat. Catal.* **2019**, *2*, 377.
[4] P. Wang, F. Chang, W. Gao, J. Guo, G. Wu, T. He, P. Chen, *Nat. Chem.* **2017**, *9*, 64.
[5] S. L. Foster, S. I. P. Bakovic, R. D. Duda, S. Maheshwari, R. D. Milton, S. D. Minteer, M. J. Janik, J. N. Renner, L. F. Greenlee, *Nat. Catal.* **2018**, *1*, 490.
[6] J. Deng, J. A. Iñiguez, C. Liu, *Joule* **2018**, *2*, 846.
[7] G. F. Chen, S. Ren, L. Zhang, H. Cheng, Y. Luo, K. Zhu, L. X. Ding, H. Wang, *Small Methods* **2019**, *3*, 1800337.
[8] P. H. van Langevelde, I. Katsounaros, M. T. Koper, *Joule* **2021**, *5*, 290.
[9] D. Hao, Z.-g. Chen, M. Figiela, I. Stepniak, W. Wei, B.-J. Ni, *J. Mater. Sci. Technol.* **2021**, *77*, 163.
[10] Y. Zeng, C. Priest, G. Wang, G. Wu, *Small Methods* **2020**, *4*, 2000672.
[11] G.-F. Chen, Y. Yuan, H. Jiang, S.-Y. Ren, L.-X. Ding, L. Ma, T. Wu, J. Lu, H. Wang, *Nat. Energy* **2020**, *5*, 605.
[12] J. Li, G. Zhan, J. Yang, F. Quan, C. Mao, Y. Liu, B. Wang, F. Lei, L. Li, A. W. Chan, *J. Am. Chem. Soc.* **2020**, *142*, 7036.
[13] Z.-Y. Wu, M. Karamad, X. Yong, Q. Huang, D. A. Cullen, P. Zhu, C. Xia, Q. Xiao, M. Shakouri, F.-Y. Chen, *Nat. Commun.* **2021**, *12*, 2506.
[14] P. Li, Z. Jin, Z. Fang, G. Yu, *Energy Environ. Sci.* **2021**, *14*, 3522.
[15] N. Zhang, J. Shang, X. Deng, L. Cai, R. Long, Y. Xiong, Y. Chai, *ACS Nano* **2022**, *16*, 4795.
[16] Y. Wang, A. Xu, Z. Wang, L. Huang, J. Li, F. Li, J. Wicks, M. Luo, D.-H. Nam, C.-S. Tan, *J. Am. Chem. Soc.* **2020**, *142*, 5702.
[17] W. He, J. Zhang, S. Dieckhöfer, S. Varhade, A. C. Brix, A. Lielpetere, S. Seisel, J. R. Junqueira, W. Schuhmann, *Nat. Commun.* **2022**, *13*, 1.
[18] H. Liu, X. Lang, C. Zhu, J. Timoshenko, M. Rüscher, L. Bai, N. Guijarro, H. Yin, Y. Peng, J. Li, *Angew. Chem.* **2022**, *61*, 202202556.
[19] Q. Liu, L. Xie, J. Liang, Y. Ren, Y. Wang, L. Zhang, L. Yue, T. Li, Y. Luo, N. Li, *Small* **2022**, *18*, 2106961.
[20] S. Ye, Z. Chen, G. Zhang, W. Chen, C. Peng, X. Yang, L. Zheng, Y. Li, X. Ren, H. Cao, *Energy Environ. Sci.* **2022**, *15*, 760.
[21] C. L. Ford, Y. J. Park, E. M. Matson, Z. Gordon, A. R. Fout, *Science* **2016**, *354*, 741.
[22] M. Duca, J. R. Weeks, J. G. Fedor, J. H. Weiner, K. A. Vincent, *ChemElectroChem* **2015**, *2*, 1086.
[23] R. D. Milton, S. D. Minteer, *ChemPlusChem* **2017**, *82*, 513.
[24] Y. Xiao, S. Vanka, T. A. Pham, W. J. Dong, Y. Sun, X. Liu, I. A. Navid, J. B. Varley, H. Hajibabaei, T. W. Hamann, *Nano Lett.* **2022**, *22*, 2236.
[25] W. J. Dong, P. Zhou, Y. Xiao, I. A. Navid, J.-L. Lee, Z. Mi, *ACS Catal.* **2022**, *12*, 2671.
[26] S. Vanka, E. Arca, S. Cheng, K. Sun, G. A. Botton, G. Teeter, Z. Mi, *Nano Lett.* **2018**, *18*, 6530.
[27] H. E. Kim, J. Kim, E. C. Ra, H. Zhang, Y. J. Jang, J. S. Lee, *Angew. Chem., Int. Ed.* **2022**, *61*, 202204117.
[28] W. J. Dong, K. W. Lim, H. W. Cho, C. J. Yoo, J. Ham, W. S. Cho, J. Y. Park, J.-L. Lee, *ACS Appl. Energy Mater.* **2024**, *7*, 6569.
[29] W. J. Dong, Y. Xiao, K. R. Yang, Z. Ye, P. Zhou, I. A. Navid, V. S. Batista, Z. Mi, *Nat. Commun.* **2023**, *14*, 179.
[30] W. J. Dong, Z. Ye, S. Tang, I. A. Navid, Y. Xiao, B. Zhang, Y. Pan, Z. Mi, *Adv. Sci.* **2024**, *11*, 2309548.
[31] Y. Xiao, X. Kong, S. Vanka, W. J. Dong, G. Zeng, Z. Ye, K. Sun, I. A. Navid, B. Zhou, F. M. Toma, *Nat. Commun.* **2023**, *14*, 2047.
[32] S. Wolter, B. Luther, D. Waltemyer, C. Önneby, S. E. Mohney, R. Molnar, *Appl. Phys. Lett.* **1997**, *70*, 2156.
[33] T. Duan, J. Pan, D. S. Ang, *Appl. Phys. Lett.* **2013**, *102*, 201604.
[34] Z. Jiang, W. Zhang, L. Jin, X. Yang, F. Xu, J. Zhu, W. Huang, *J. Phys. Chem. C* **2007**, *111*, 12434.
[35] W. J. Dong, I. A. Navid, Y. Xiao, T. H. Lee, J. W. Lim, D. Lee, H. W. Jang, J.-L. Lee, Z. Mi, *J. Mater. Chem. A* **2022**, *10*, 7869.
[36] W. J. Dong, I. A. Navid, Y. Xiao, J. W. Lim, J.-L. Lee, Z. Mi, *J. Am. Chem. Soc.* **2021**, *143*, 10099.
[37] S. Vanka, B. Zhou, R. A. Awni, Z. Song, F. A. Chowdhury, X. Liu, H. Hajibabaei, W. Shi, Y. Xiao, I. A. Navid, *ACS Energy Lett.* **2020**, *5*, 3741.
[38] J. Tan, B. Kang, K. Kim, D. Kang, H. Lee, S. Ma, G. Jang, H. Lee, J. Moon, *Nat. Energy* **2022**, *7*, 537.
[39] W. J. Dong, J. P. Menzel, Z. Ye, I. A. Navid, P. Zhou, K. R. Yang, V. S. Batista, Z. Mi, *ACS Catal.* **2024**, *14*, 2588.
[40] W. J. Dong, J. P. Menzel, K. Li, Z. Ye, Z. Long, I. A. Navid, K. R. Yang, Y. Xiao, V. S. Batista, Z. Mi, *Nat. Commun.*